

Tuning of charge density wave transitions in LaAu_xSb_2 by pressure and Au stoichiometry

Li Xiang ^{1,2}, Dominic H. Ryan,^{1,2,3} Warren E. Straszheim ¹, Paul C. Canfield,^{1,2} and Sergey L. Bud'ko ^{1,2}

¹Ames Laboratory, US DOE, Iowa State University, Ames, Iowa 50011, USA

²Department of Physics and Astronomy, Iowa State University, Ames, Iowa 50011, USA

³Physics Department and Centre for the Physics of Materials, McGill University, 3600 University Street, Montreal, Quebec, Canada H3A 2T8

 (Received 20 May 2020; revised 17 August 2020; accepted 25 August 2020; published 8 September 2020)

Two charge density wave transition can be detected in LaAuSb_2 at ~ 110 and ~ 90 K by careful electrical transport measurements. Whereas control of the Au site occupancy in LaAu_xSb_2 (for $0.9 \lesssim x \lesssim 1.0$) can suppress each of these transitions by ~ 80 K, the application of hydrostatic pressure can completely suppress the lower transition by ~ 7.5 kbar and the upper transition by ~ 17 kbar. Clear anomalies in the resistance as well as the magnetoresistance are observed to coincide with the pressures at which the charge density wave transitions are driven to zero.

DOI: [10.1103/PhysRevB.102.125110](https://doi.org/10.1103/PhysRevB.102.125110)

I. INTRODUCTION

Charge density wave (CDW) phenomena continue to attract the attention of condensed matter physicists [1–5]. One of the fascinating research lines continues to be coexistence and competition of CDW and other collective phenomena like superconductivity [6–10]. On a more basic level though, despite more than half a century history [11–13], the driving forces for CDW formation in different materials as well as classification of CDWs are still under discussion [1–3]. In this context, the identification and studies of new CDW materials are important to diversify the pool of well-studied systems.

Ternary LaAgSb_2 [14,15] is a nonmagnetic member of the family of tetragonal (ZrCuSi_2 structure type, space group $P4/nmm$) RAgSb_2 (R = rare earth) compounds with diverse physical properties [15,16]. The anomalies in many physical properties [16–21] suggested formation of two CDWs in LaAgSb_2 , one at $T_{\text{CDW1}} = 208$ K and another at $T_{\text{CDW2}} = 186$ K. X-ray diffraction studies have provided direct evidence of CDW formations below T_{CDW1} [along the a direction with $\tau_1 = 0.026(2\pi/a)$] and below T_{CDW2} [along the c direction with $\tau_2 = 0.16(2\pi/c)$] [17], with the Fermi surface nesting being suggested as the origin of these CDWs. Moreover, LaAgSb_2 was proposed to have Dirac states with a close relationship between the Dirac cone to the CDW ordering [22,23].

Effects of rare-earth substitution [24,25] and hydrostatic pressure [24,26] on the temperature of the higher CDW transition, T_{CDW1} were studied. The observed suppression of the T_{CDW1} was explained as a combination of increase of the three-dimensional character of LaAgSb_2 (decrease of c/a value) and the substitution-related disorder. It was also recognized that the pressure response of T_{CDW1} could be affected by local moment magnetism as well as hybridization due to rare-earth ($R = \text{Ce}, \text{Pr}, \text{Nd}, \dots$) substitution in $(\text{La}_{1-x}\text{R}_x)\text{AgSb}_2$ [26].

Less than a decade ago, CDW formation at ~ 95 K was reported, even if in passing, for a closely related material,

LaAuSb_2 [27]. This work was followed by recent (magneto-) electrical and thermal transport studies, as well as ultrafast pump-probe spectroscopy measurements, on LaAuSb_2 [28] providing evidence for partial gapping of the Fermi surfaces during the CDW transition at around 88 K. Additionally, resistivity data for several samples of the $\text{La}(\text{Ag}_{1-x}\text{Au}_x)\text{Sb}_2$ series were reported [25], indicating suppression of the CDW transition with Au substitution (only one CDW transition was detected). In this work the Au-end compound had $T_{\text{CDW}} = 88$ K and was designated as $\text{LaAu}_{0.88}\text{Sb}_2$.

Indeed, in contrast to the stoichiometric RAgSb_2 series [16,29], the RAuSb_2 family (in particular more thoroughly studied CeAuSb_2) was suspected to have transition metal deficiency [27,30]. Different Au occupancies, x , on the single Au site, Au 2b, are most probably responsible for different values of the observed T_{CDW} as well as the range of residual resistivity ratios (RRR) in LaAu_xSb_2 [25,27,28].

Having in mind apparent similarity between LaAu_xSb_2 and the much more studied LaAgSb_2 as well as the additional complexity of the former material due to its transition metal deficiency, in this work we aim to address several questions: (a) can we tune and control Au occupancy x in LaAu_xSb_2 ? (b) as in the case of LaAgSb_2 , is there a second, lower temperature CDW in LaAu_xSb_2 ? (c) how are the CDW transitions affected by x ? (d) is the pressure response of the CDW transitions in LaAu_xSb_2 different from those in LaAgSb_2 ? (e) will we be able to suppress the CDW transitions in LaAu_xSb_2 completely, and if so, are there any anomalies in (magneto-) transport associated with the CDW quantum phase transitions/quantum critical points?

II. EXPERIMENTAL DETAILS

Single crystals of LaAu_xSb_2 were grown from an antimony-rich self-flux following the method described in Refs. [16,30]. 5–6 grams of the pure elements were loaded into the lower (growth) half of an alumina Canfield crucible

set [31], which was capped with an alumina frit and a second (catch) alumina crucible. This assembly was loaded into an amorphous silica tube, evacuated, backfilled to ~ 150 mbar with argon, and sealed. The sealed tubes were heated to 1050°C over a period of 10 h, held for 8 h to ensure the formation of a homogeneous liquid, then cooled to 800°C over a period of 10 h prior to starting the crystal growth (we found no solids down to 750°C). Crystal growth occurred during the 100 h cooling from 800 to 670°C , after which the excess flux was removed using a centrifuge. Typical yields were 500 mg–600 mg as 1–3 well-faceted crystals, ~ 5 mm on each side and ~ 1 -mm thick.

To investigate whether reported Au deficiency [25,27] was affected and could be tuned by the initial stoichiometry of the melt, five initial La : Au : Sb growth compositions were used: 1 : 1 : 20 (denoted Au1), 1 : 2 : 20 (Au2), 1 : 4 : 20 (Au4), 1 : 6 : 20 (Au6), and 1 : 8 : 20 (Au8). Similar excess of Au was found to yield near stoichiometric (as measured by energy dispersive spectroscopy) CeAuSb_2 ; initial Ce : Au : Sb ratios of 1 : 6 : 12 (Ref. [30]) gave residual resistivity ratios between 6 and 9, quite similar to our findings for Au6 and Au8 growths as shown below. The excess Au in the starting melt did not appear to adversely affect the size of the final crystals, however we observed slightly more surface contamination by flux (a mixture of Sb and AuSb_2) in the higher Au-derived samples.

Cu- K_α x-ray diffraction patterns were taken for all of the samples using a Rigaku Miniflex-II diffractometer. For each starting growth composition the crystal was cleaned to remove any residual flux (mechanical scraping followed by wiping with an ethanol-soaked paper tissue) then a small piece was broken off and hand ground under ethanol to minimize oxidation. The powder was mounted on a low-background single-crystal silicon plate using a trace amount of Dow Corning silicone vacuum grease. The mount was spun during data collection to reduce possible effects of texture. Data taken for Rietveld refinement were collected in two overlapping blocks $10^\circ \leq 2\theta \leq 48^\circ$ and $38^\circ \leq 2\theta \leq 100^\circ$, with the second block counted for 4–5 times longer than the first to compensate for the loss of scattered intensity at higher angles due to the x-ray form factors. This strategy typically yielded ~ 10 Bragg

reflections with intensities over 2000 counts and many other statistically significant reflections out to $2\theta = 100^\circ$ allowing us to decouple the effects of site occupation and thermal factors in the structural analysis. The diffractometer and analysis procedures were checked using Al_2O_3 (SRM 676a [32]) and our fitted values of $a = 4.7586(2)$ Å and $c = 12.9903(7)$ Å were both $1.6(4) \times 10^{-4}$ smaller than the values on the certificate [32], suggesting a small but statistically significant miscalibration of the instrument. The fitted lattice parameters given in the analysis that follows do not include this correction.

Standard, linear four-probe ac resistivity was measured on bar-shaped samples of LaAu_xSb_2 in two arrangements: $I||ab$ and, when needed, $I||c$. The frequency used was 17 Hz, typical current values were 3 mA for in-plane electrical transport and 5 mA for the c -axis measurements. Magnetoresistance was measured in a transverse configuration: $H||c$ for the in-plane transport and $H||ab$ for $I||c$. The measurements were performed using the ACT option of a Quantum Design Physical Property Measurement System (PPMS).

For selected samples, resistivity measurements under pressure were performed in a hybrid, BeCu / NiCrAl piston-cylinder pressure cell (modified version of the one used in Ref. [33]) in the temperature and magnetic field environment provided by a PPMS instrument. A 40 : 60 mixture of light mineral oil and n-pentane was used as a pressure-transmitting medium. This medium solidifies at room temperature in the pressure range of 30–40 kbar [33–35], which is above the maximum pressure in this work. Elemental Pb was used as a low temperature pressure gauge [36]. It has been shown [37–39] that in piston-cylinder pressure cells high temperature pressures are different from low temperature pressures. Given that the transitions of interest occur below ~ 115 K (see below), here we simply use the Pb gauge pressure value. This may give rise to pressure differences with the values determined by Pb gauge by at most few tenths of a kbar.

Note, that for $\text{LaAu}_{0.970}\text{Sb}_2$ ρ_c has been measured both at ambient pressure and under pressure, however it appears that a small crack has developed in the sample during assembling and closing of the pressure cell, causing some inconsistency between the ambient pressure and the lowest pressure data.

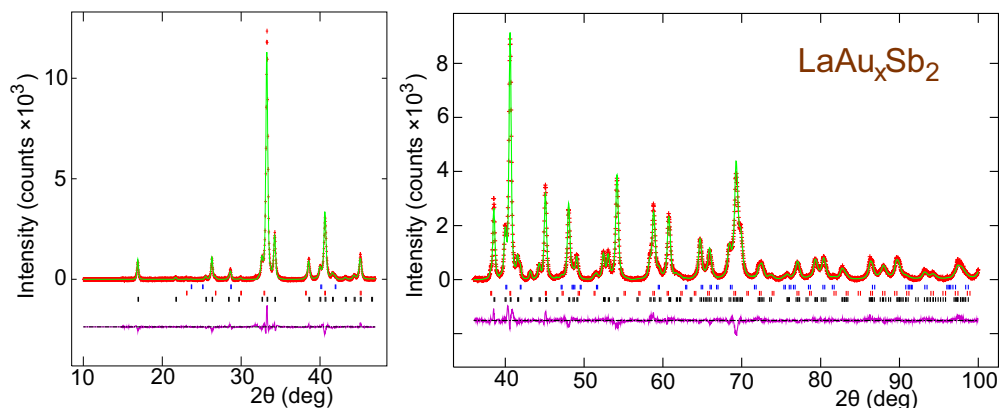


FIG. 1. Cu- K_α x-ray diffraction patterns for the Au4 growth of LaAu_xSb_2 showing the two overlapping data blocks that were cofitted using the GSAS/EXPGUI packages [40,41]. The red points are the data and the green lines show the fits with the residuals shown below each fitted pattern. The Bragg markers show the positions of the reflections from (top) Sb, (middle) AuSb_2 and (bottom) LaAu_xSb_2 .

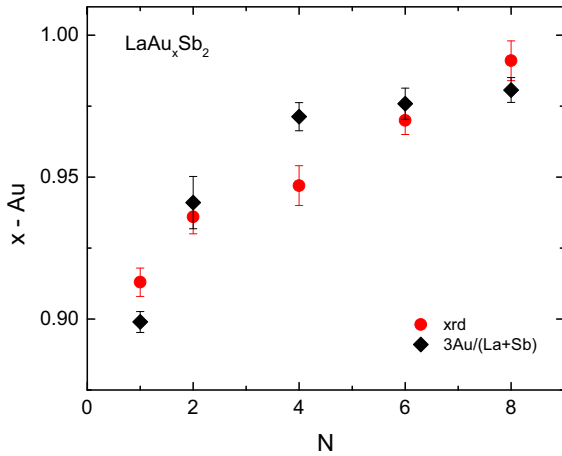


FIG. 2. The fitted occupation of the Au site (red circles) in LaAu_xSb_2 as a function of N , in starting stoichiometry 1 (La) : N (Au) : 20 (Sb), plotted together with Au concentration relatively to (La + Sb) (black diamonds) determined from EDS measurements.

The ambient pressure data is not included in Figs. 11(b) and 12(c).

Chemical analysis of the crystals was performed using an Oxford Instruments energy-dispersive x-ray spectroscopy (EDS) system on a Thermo Scientific Teneo scanning electron microscope. The measurements were performed on polished ab surfaces of single crystals with four points taken for every sample.

III. RESULTS

A. Tuning and control of Au concentration in LaAu_xSb_2

The x-ray diffraction patterns were fitted using the GSAS/EXPGUI packages [40,41]. Small amounts of residual flux were generally observed as impurity phases and were included in the fits as necessary. Figure 1 shows a typical x-ray diffraction data set for the Au4 growth of LaAuSb_2 with 1.7 wt.% AuSb_2 and 3.2 wt.% Sb as impurities. In the fit, the occupation of the Au $2b$ site was allowed to vary and was

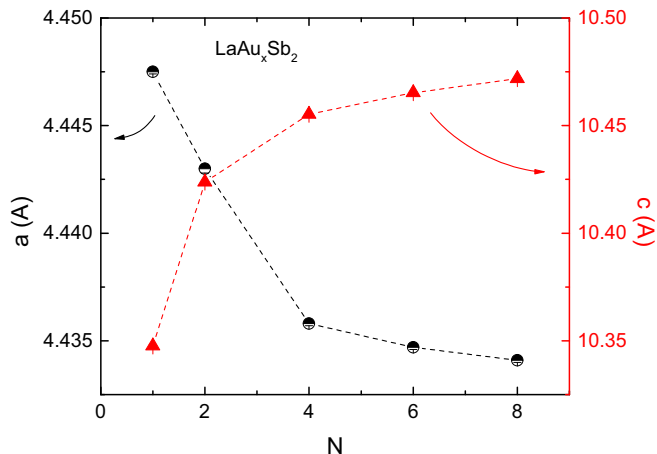


FIG. 3. Lattice parameters a and c of LaAu_xSb_2 plotted as a function of N , in starting stoichiometry 1 (La) : N (Au) : 20 (Sb).

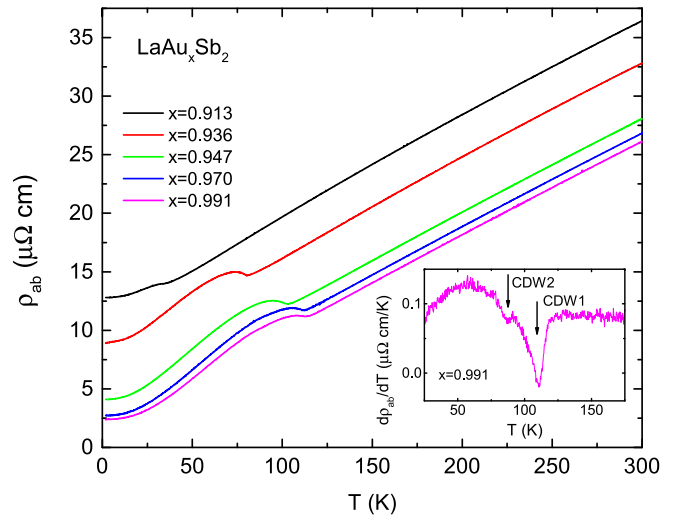


FIG. 4. Temperature-dependent, in-plane, resistivity data for the $x = 0.970$ sample together with resistance data for the other LaAu_xSb_2 samples normalized to that of the $x = 0.970$ sample so that the room temperature slope of the $\rho_{ab}(T)$ data match (see text for details). Inset: temperature derivative of resistivity for $\text{LaAu}_{0.991}\text{Sb}_2$, arrows mark two CDW transitions.

found to be less than one (see below), whereas the occupations of La, Sb1, and Sb2 sites were fixed as 1. The results of the Rietveld analysis of the powder x-ray data for all 5 LaAu_xSb_2 samples are listed in Tables I and II in Appendix A.

The EDS results for the 5 LaAu_xSb_2 samples are presented in Table III in Appendix A. The values in the table are the average of the measurements taken at four different places on the samples' surfaces, standard deviations are listed in the parentheses.

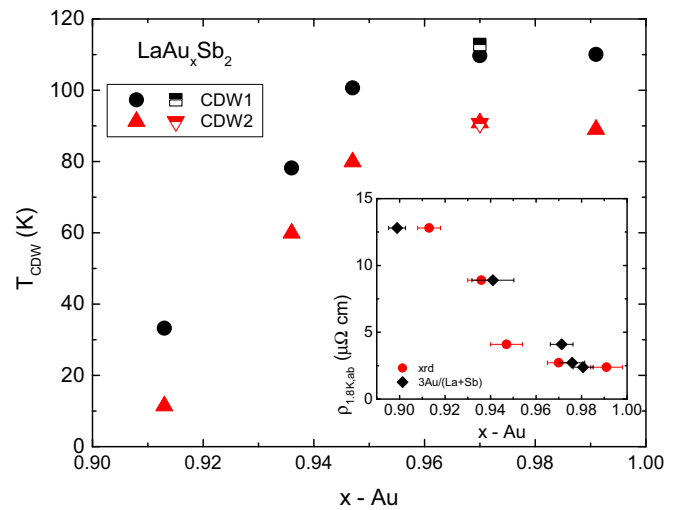


FIG. 5. CDW transition temperatures, T_{CDW1} and T_{CDW2} as a function of x determined by Rietveld refinement in LaAu_xSb_2 . Filled and half-filled symbols-from in-plane and c -axis resistivity data respectively. Inset: residual resistivity, $\rho_{1.8\text{K},ab}$ as a function of x determined from x-ray diffraction (red circles) and EDS (black diamonds).

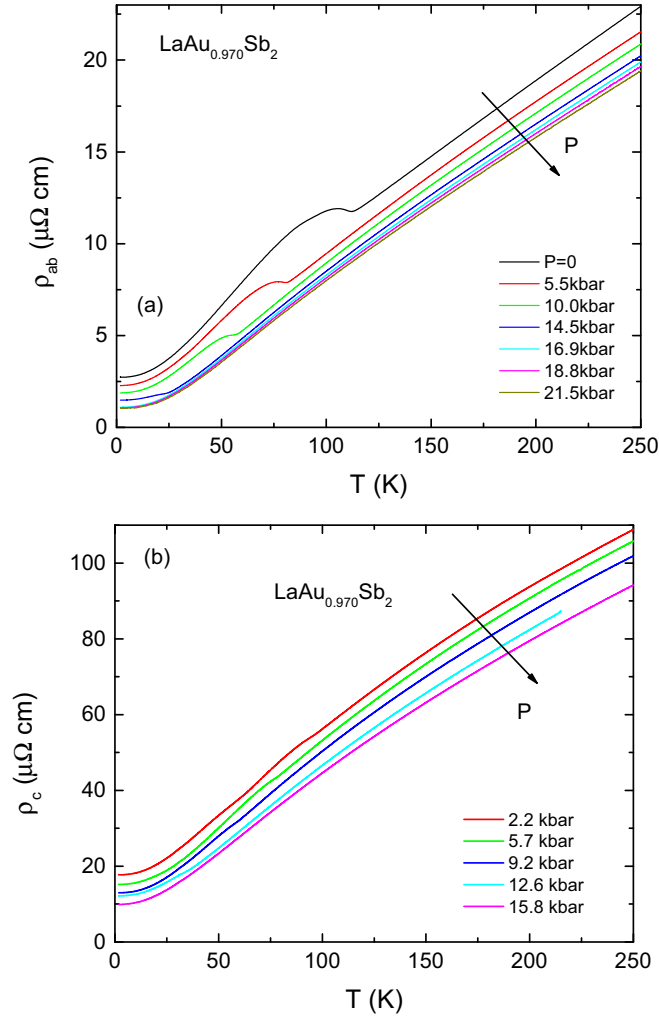


FIG. 6. Temperature-dependent (a) in-plane, (b) c -axis resistivity of $\text{LaAu}_{0.970}\text{Sb}_2$ measured at different pressures. Arrows point to the direction of pressure increase.

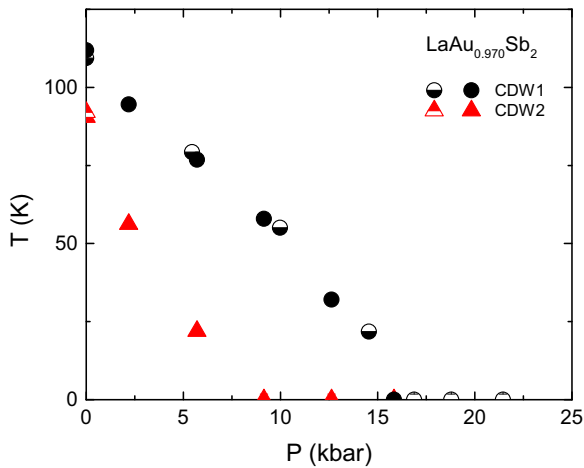


FIG. 7. Pressure - temperature phase diagram of $\text{LaAu}_{0.970}\text{Sb}_2$. Half-filled and filled symbols are from $I||ab$ and $I||c$ runs, respectively. Symbols at $T = 0$ correspond to pressures at which no anomalies were detected above 1.8 K.

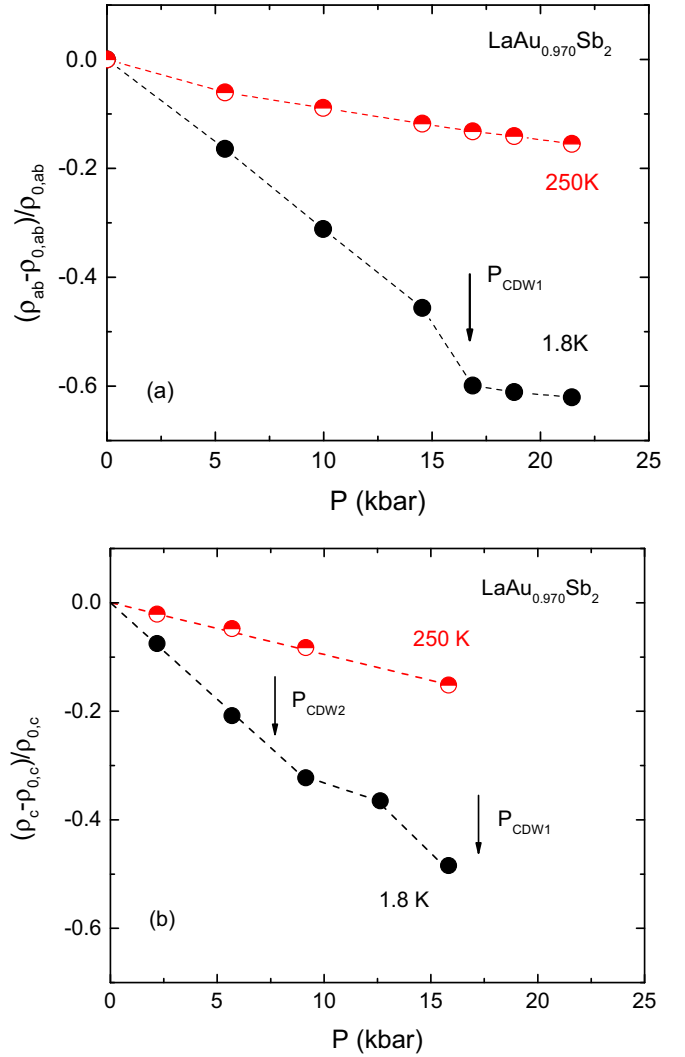


FIG. 8. Relative change of (a) in-plane and (b) c -axis resistivity of $\text{LaAu}_{0.970}\text{Sb}_2$ at 250 K and 1.8 K under pressure. Arrow marks critical pressures for CDW1 and CDW2 suppression.

Analysis of the x-ray diffraction as well as EDS results clearly show that increasing the gold content of the starting mixture had a significant effect on the Au occupancy of the grown crystals. The fitted occupation of the Au $2b$ site increased from 0.913(5) for Au1 to 0.991(7) by Au8. This span of Au concentrations is consistent with the EDS data. The Au occupancy from the x-ray diffraction and atomic ratio of $3\text{Au}/(\text{La} + \text{Sb})$ from the EDS data are plotted together in Fig. 2. The largest increase of the Au concentration appears to happen between the Au1 and Au4 samples, followed by almost saturation for Au6 and Au8. This saturation effect is also clearly visible in the behavior of the lattice parameters shown in Fig. 3. While we do observe vacancies on the Au site, the Au occupancy determined in this study is above the 0.88 reported by Masubuchi *et al.* [25] for the Au2 sample that should correspond to the composition that they used. Our Au6 and Au8 samples are within composition range reported for CeAu_xSb_2 grown with Ce : Au of 1 : 6. [30].

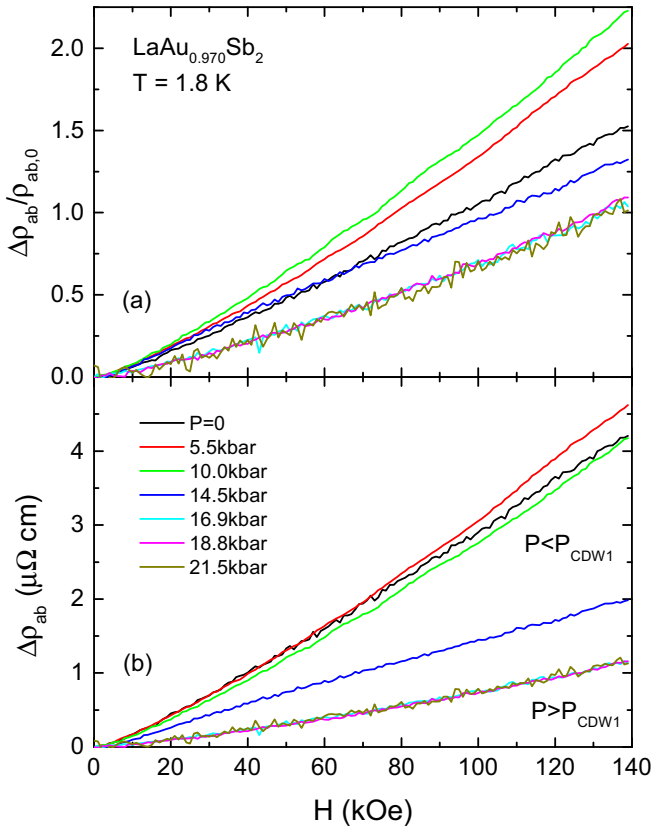


FIG. 9. (a) Transverse magnetoresistance, $\Delta\rho_{ab}/\rho_{ab,0} = [\rho_{ab}(H) - \rho_{ab}(H=0)]/\rho_{ab}(H=0)$, ($I\parallel ab, H\parallel c$), and (b) change in resistivity in applied magnetic field, $\Delta\rho_{ab} = \rho_{ab}(H) - \rho_{ab}(H=0)$, ($I\parallel ab, H\parallel c$) of $\text{LaAu}_{0.970}\text{Sb}_2$ at 1.8 K measured under pressure up to 21.5 kbar.

In the rest of the text we will use the notation LaAu_xSb_2 with x determined from the Rietveld refinement of the powder x-ray data.

B. Ambient pressure electrical transport and CDW transitions

Temperature-dependent, in-plane, resistivity data for the $x = 0.970$ ($N = 6$) sample is shown in Fig. 4. Given the uncertainty in geometric factors of the resistance bars, we have normalized the resistance data (multiplicatively) for the other LaAu_xSb_2 samples to that of the $x = 0.970$ ($N = 6$) sample so that the room temperature slope of the $\rho_{ab}(T)$ data match. This normalization is premised on the ansatz that small changes in Au occupancy will not change the phonon spectra at 300 K (i.e., the electron phonon scattering that dominates the temperature dependent resistivity at 300 K) in any significant manner. The data shown in Fig. 4 preserve the RRR values and also demonstrate very clear Matthiessen's rule offsets of the higher temperature ($T > T_{\text{CDW}}$) resistivity. (The same ρ_{ab} resistivity data normalized to the values at 300 K and the RRR values as a function of x are shown in the Appendix B.) Remarkably, the ρ_0 values (inset to Fig. 5) vary as $\sim 1 \mu\Omega \text{ cm}$ per percent Au vacancy; this is consistent with the very gross, textbook rule of thumb [42] for residual resistivity given for generic metallic samples. We clearly detect two CDW transitions, a higher temperature CDW1 and a lower temperature CDW2. CDW1 is

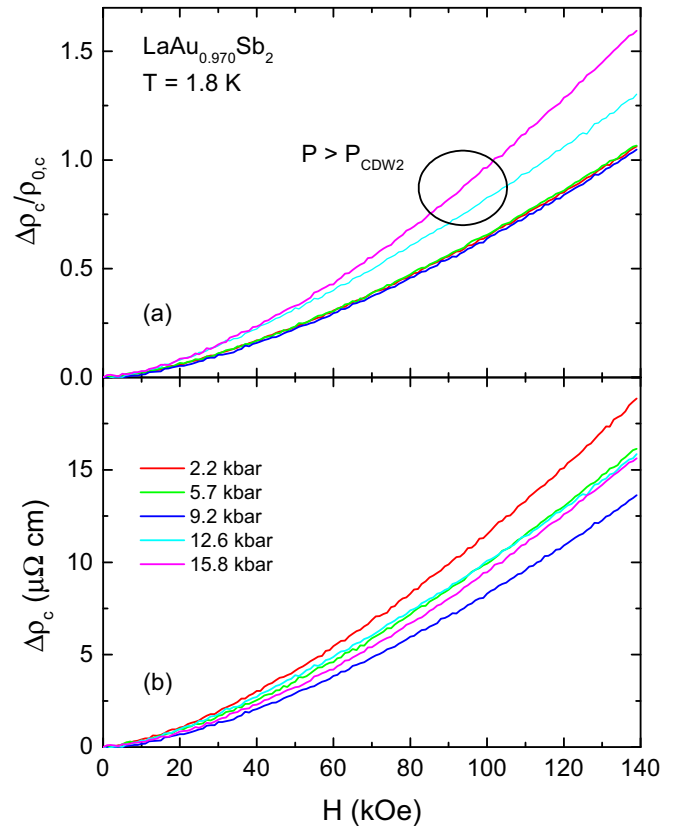


FIG. 10. (a) Transverse magnetoresistance ($I\parallel c, H\parallel ab$), and (b) change in resistivity in applied magnetic field ($I\parallel c, H\parallel ab$) of $\text{LaAu}_{0.970}\text{Sb}_2$ at 1.8 K measured under pressure up to 15.8 kbar.

easily identified in in-plane resistivity measurements (Fig. 4). For some of the Au concentrations the lower, CDW2 transition, is seen in the temperature derivatives of the ρ_{ab} , as shown, for example in the inset to Fig. 4. For the $x = 0.970$ sample $I\parallel c, \rho_c(T)$, measurements were performed to observe CDW2 more clearly. As was previously observed for pure LaAgSb_2 [16,17], by the combination of in-plane and c -axis resistivity measurements, two CDW transitions were detected for all five x concentrations in LaAu_xSb_2 .

The CDW temperatures of LaAu_xSb_2 , T_{CDW1} and T_{CDW2} , are plotted in Fig. 5 as a function of the Au site occupancy x determined from the Rietveld refinement of the powder x-ray diffraction spectra. As it was observed for the lattice parameters, the main change in the CDW temperatures happens between $x = 0.913$ and $x = 0.947$ (samples Au1-Au4).

C. Electrical transport under pressure, CDW quantum critical point

For measurements of electrical properties under pressure we have chosen $\text{LaAu}_{0.970}\text{Sb}_2$ as a sample with Au site almost fully occupied. (For comparison, in Appendix E, we present similar data from measurements on $\text{LaAu}_{0.936}\text{Sb}_2$. This composition is similar in growth conditions and the value of T_{CDW1} to the samples reported in the literature at ambient pressure [25,28].)

Figure 6(a) shows in-plane resistivity of $\text{LaAu}_{0.970}\text{Sb}_2$ measured at different pressures up to 21.5 kbar. As in the

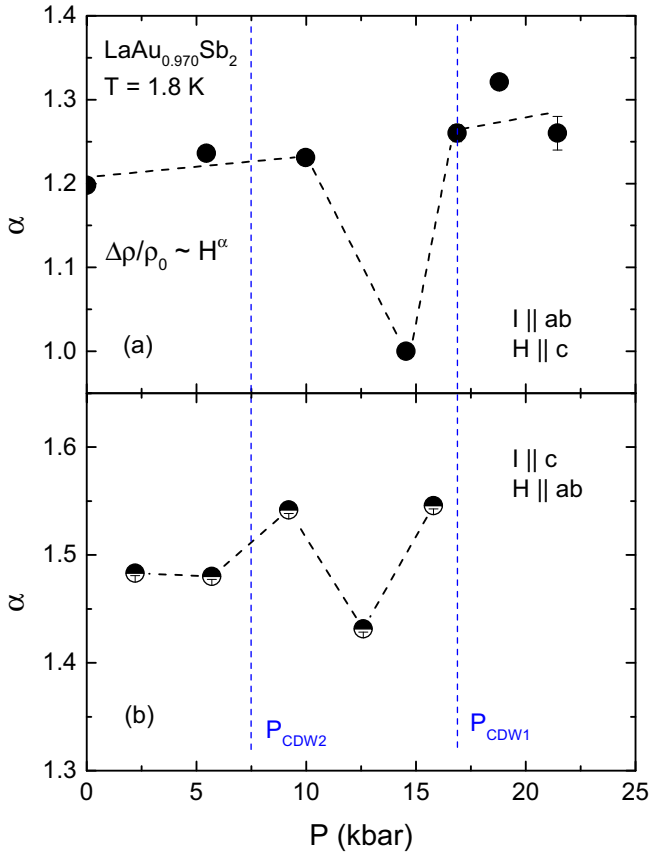


FIG. 11. Pressure dependence of the exponent α in magnetoresistance ($\Delta\rho/\rho_0 \propto H^\alpha$) (a) for $I \parallel ab, H \parallel c$, and (b) for $I \parallel c, H \parallel ab$. Dashed lines are a guide for the eye. Vertical dashed lines mark critical pressures for CDW1 and CDW2.

case of LaAgSb_2 [24,26], resistivity decreases under pressure and the feature associated with the CDW1 becomes smaller and shifts down in temperature. For the $\text{LaAu}_{0.970}\text{Sb}_2$ sample the available pressure range is enough to suppress the T_{CDW1} completely to zero. It should be noted that in this case the in-plane resistivity measurements [Fig. 6(a)] did not present a clear feature for CDW2, so a second series of pressure runs, using c -axis resistivity measurements, were performed [Fig. 6(b)]. In these ρ_c data, both transitions were detected. [The $d\rho_i/dT$ ($i = ab, c$) derivatives, near the CDW transitions, of the data shown in Figs. 6(a) and 6(b), are presented in the Appendix C]. The $P - T$ phase diagram is shown in Fig. 7. The suppression of both CDWs is close to linear in pressure. The evaluated pressure derivatives are $dT_{\text{CDW1}}/dP = -6.0(2)$ K/kbar and $dT_{\text{CDW2}}/dP = -12(2)$ K/kbar, and extrapolated critical pressures are ~ 17 and ~ 7.5 kbar for CDW1 and CDW2, respectively. For $\text{LaAu}_{0.970}\text{Sb}_2$ the higher temperature CDW is suppressed somewhat faster than for LaAgSb_2 , where the pressure derivative value of $-4.3(1)$ K/kbar has been reported [24,26].

Pressure-induced relative changes of the in-plane resistivity of $\text{LaAu}_{0.970}\text{Sb}_2$ at the base temperature, 1.8 K, and above the CDW transitions, at 250 K, are presented in Fig. 8(a). At 250 K the resistivity decreases in an almost linear fashion, with a rate of $1/\rho_0 d\rho/dP = -0.0070(4)$ 1/K, which is close

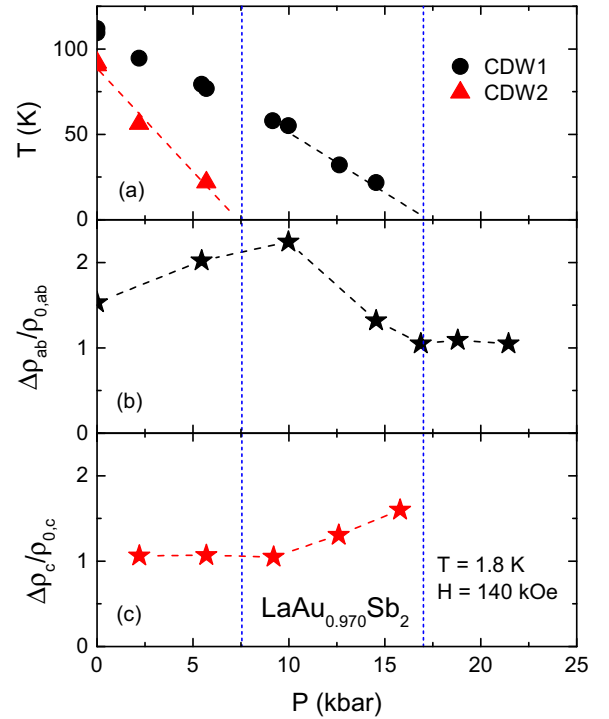


FIG. 12. (a) $P - T$ phase diagram for $\text{LaAu}_{0.970}\text{Sb}_2$. (b) and (c) magnetoresistance at $T = 1.8$ K and $H = 140$ kOe as a function of pressure for $I \parallel ab, H \parallel c$ and $I \parallel c, H \parallel ab$, respectively. Dashed lines are a guide for the eye. Vertical dashed lines mark critical pressures for CDW1 and CDW2.

to -0.0088 1/K reported for LaAgSb_2 at 300 K [26]. In contrast, the base temperature resistivity initially decreases 4–5 times faster, and then has a clear change of slope close to the critical pressure of CDW1. This is not unexpected, since below the critical pressure an additional contribution from suppression of the resistive increase associated with the CDW and its associated Fermi surface nesting plays an important role.

A similar set of data for the c -axis resistivity is shown in Fig. 8(b). The 250-K data show a close to linear decrease with a rate of $-0.0097(4)$ 1/K, that is not far from that for in-plane resistivity. Initially, the 1.8 K resistivity decreases 3–4 times faster, with a rate of $-0.036(1)$ 1/K. The 1.8 K data set has a clear anomaly close to P_{CDW2} , the critical pressure for CDW2. Unfortunately, the maximum pressure for the c -axis resistivity run was below the P_{CDW1} , so we were not able to evaluate if there is any anomaly associated with it.

The transitions from normal to CDW1 state as well as from CDW1 to CDW2 state appear to be of the second order, so the suppression of the CDW1 to $T = 0$ K could be recognized as a CDW quantum critical point. A brief discussion of the evolution of the functional behavior of the low temperature resistivity under pressure is presented in Appendix D. Here we further examine (magneto-) transport properties in the vicinity of the CDW quantum critical point (QCP) in some detail.

Transverse magnetoresistance, $\Delta\rho_{ab}/\rho_{ab,0} = [\rho_{ab}(H) - \rho_{ab}(H = 0)]/\rho_{ab}(H = 0)$, ($I \parallel ab, H \parallel c$) of $\text{LaAu}_{0.970}\text{Sb}_2$ was measured up to 140 kOe at 1.8 K [Fig. 9(a)]. It is nonsaturating and at the maximum field has respectable values between

$\sim 225\%$ and $\sim 100\%$. The data for $P \geq 16.9$ kbar basically fall on the same line. If one replots these data as change of resistivity in applied field (without normalizing by the zero field resistivity, $\Delta\rho_{ab} = \rho_{ab}(H) - \rho_{ab}(H=0)$, [Fig. 9(b)] the results are even more curious: the data are separated into two well-defined manifolds: $P < P_{\text{CDW1}}$ ($P \leq 10.0$ kbar) and $P > P_{\text{CDW1}}$ ($P \geq 16.9$ kbar) with the data taken at the pressure close to critical, $P = 14.5$ kbar, being in between these two manifolds.

Similar data for $I||c$, $H||a$ are presented in Fig. 10. Although there is not a clear segregation of the change in resistivity data, we can see that whereas the field dependent magnetoresistance for $P \leq P_{\text{CDW2}}$ scale to the same curve, the data for $P > P_{\text{CDW2}}$ appear to be clearly separate.

To quantify the evolution of the curvature of the field-dependent magnetoresistance with pressure we can replot the data from Figs. 9(a) and 10(a) on a log-log scale (see Fig. 17 in Appendix E) and perform linear fits of the data (between ~ 20 and 140 kOe). Resulting slopes that are exponents α in $\Delta\rho/\rho_0 \propto H^\alpha$ are plotted as a function of pressure in Fig. 11 for in-plane and c -axis resistivity data. Indeed, there is a clear change in the exponents α near the critical pressures for CDW2 and CDW1.

Another parameter to follow is the value of magnetoresistance at 140 kOe as a function of pressure. This parameter entangles zero-field resistivity and the functional dependence of magnetoresistance on the applied field. Surprisingly, it appears that for ρ_{ab} data this parameter displays anomalies associated with suppression of both CDW1 and CDW2, not just the dominant CDW1 [Fig. 12(b)]. For the ρ_c data an anomaly at T_{CDW2} is clearly seen [Fig. 12(c)].

IV. SUMMARY

In this work we were able to tune and control Au occupancy in LaAu_xSb_2 single crystals by changing the initial concentration of the elements in the melt. The value of x varied from $x = 0.913(5)$ to $x = 0.991(7)$, using values of x from Au site occupancy obtained in the Rietveld refinement of the powder x-ray data. For all the samples in this Au concentration range two CDWs were observed in the combination of in-plane and c -axis electrical transport. The CDW temperatures decrease monotonically from $T_{\text{CDW1}} = 110$ K and $T_{\text{CDW2}} = 90$ K for $x = 0.991$ to $T_{\text{CDW1}} = 33$ K and $T_{\text{CDW2}} = 11.5$ K for $x = 0.913$. This behavior is in general agreement with the expected effect of nonmagnetic impurities (or increase of nonmagnetic scattering) on CDW discussed in the literature, Refs. [43–46], combined with some contribution from the chemical pressure due to the unit cell volume decrease with decrease of x (see Appendix G for further discussion). A (small) change in band filling related to Au site occupancy could contribute to the change in CDW temperatures as well.

The CDW temperatures are suppressed under pressure. For $\text{LaAu}_{0.970}\text{Sb}_2$ a CDW QCP associated with the suppression of T_{CDW1} to zero occurs at ~ 17 kbar. Anomalies in pressure dependence of the base temperature resistivity and transverse magnetoresistance (including via the exponent α of $\Delta\rho/\rho_0 \propto H^\alpha$) are observed at the CDW QCP. The in-plane magnetoresistance measured at 1.8 K and 140 kOe has clear anomalies

at two critical pressure values, when either CDW1 or CDW2 are suppressed to $T = 0$ K. For the c -axis magnetoresistance an anomaly at P_{CDW2} is clearly observed, whereas P_{CDW1} is beyond the pressure range of the measurements. The behavior of magnetoresistance at CDW QCP requires further experimental and theoretical studies.

We did not observe the appearance of superconductivity in the pressure range where the charge density wave was suppressed. If the superconducting state indeed forms upon suppression of CDWs in LaAu_xSb_2 , experimentally there are several reasons that could preclude its observation, in particular, relatively high base temperature (1.8 K) and some disorder on the Au site.

All in all, this work presents two ways of tuning charge density waves in an intermetallic crystals, opening the door for further, detailed studies of the CDW phenomenon in general as well as its realization in LaAu_xSb_2 in particular. These studies would hopefully include synchrotron x-ray diffraction, scanning tunneling spectroscopy, and angular-resolved photoemission spectroscopy.

ACKNOWLEDGMENTS

The authors thank E. Gati and R. A. Ribeiro for useful discussions, and A. Elbakyan for assistance in literature searches. Work at the Ames Laboratory was supported by the US Department of Energy, Office of Science, Basic Energy Sciences, Materials Sciences and Engineering Division. The Ames Laboratory is operated for the US Department of Energy by Iowa State University under Contract No. DE-AC02-07CH11358. L.X. was supported, in part, by the W. M. Keck Foundation. Much of this work was carried out while D.H.R. was on sabbatical at Iowa State University and Ames Laboratory and their generous support (again under under Contract No. DE-AC02-07CH11358) during this visit is gratefully acknowledged. D.H.R. was supported as well by Fonds Québécois de la Recherche sur la Nature et les Technologies.

APPENDIX A: RIETVELD REFINEMENT AND EDS RESULTS

This Appendix contains tables with the results of Rietveld refinements and EDS chemical analysis of five LaAu_xSb_2 samples.

TABLE I. Lattice parameters of LaAu_xSb_2 samples grown using different starting compositions.

Sample	a (Å)	c (Å)	V (Å ³)
Au1	4.4475(1)	10.3476(6)	204.68(1)
Au2	4.4430(2)	10.4237(4)	205.77(1)
Au4	4.4358(1)	10.4552(3)	205.72(1)
Au6	4.4347(1)	10.4653(3)	205.81(1)
Au8	4.4341(1)	10.4718(4)	205.88(1)

TABLE II. Atomic coordinates, occupancy, and isotropic displacement parameters of LaAu_xSb_2 samples grown using different starting compositions.

Sample	atom	site	x	y	z	occupancy	U_{eq}
Au1	La	$2c$	0.25	0.25	0.2496(2)	1	0.0340(7)
	Au	$2b$	0.75	0.25	0.5	0.913(5)	0.0378(6)
	Sb1	$2a$	0.75	0.25	0	1	0.0378(6)
	Sb2	$2c$	0.25	0.25	0.6664(2)	1	0.0378(6)
Au2	La	$2c$	0.25	0.25	0.2488(3)	1	0.0288(7)
	Au	$2b$	0.75	0.25	0.5	0.936(6)	0.0311(8)
	Sb1	$2a$	0.75	0.25	0	1	0.0309(7)
	Sb2	$2c$	0.25	0.25	0.6693(2)	1	0.0309(7)
Au4	La	$2c$	0.25	0.25	0.2478(2)	1	0.0334(7)
	Au	$2b$	0.75	0.25	0.5	0.947(6)	0.0331(6)
	Sb1	$2a$	0.75	0.25	0	1	0.0344(6)
	Sb2	$2c$	0.25	0.25	0.6700(2)	1	0.0344(6)
Au6	La	$2c$	0.25	0.25	0.2465(2)	1	0.0337(6)
	Au	$2b$	0.75	0.25	0.5	0.970(5)	0.0346(5)
	Sb1	$2a$	0.75	0.25	0	1	0.0355(5)
	Sb2	$2c$	0.25	0.25	0.6703(2)	1	0.0355(5)
Au8	La	$2c$	0.25	0.25	0.2475(2)	1	0.0252(7)
	Au	$2b$	0.75	0.25	0.5	0.991(7)	0.0282(7)
	Sb1	$2a$	0.75	0.25	0	1	0.0252(6)
	Sb2	$2c$	0.25	0.25	0.6704(2)	1	0.0252(6)

APPENDIX B: NORMALIZED RESISTIVITY OF LaAu_xSb_2 AT AMBIENT PRESSURE AND TEMPERATURE DERIVATIVES OF THE DATA

Figure 13 shows the data from Fig. 4, plotted in a more traditional way, normalized to the resistivity values at $T = 300$ K. As expected, the RRR are smaller for the LaAu_xSb_2 with higher Au deficiency (lower x values). It should be noted, though, that this normalization produces a potentially unphysical change in the high temperature slopes of the $R(T)$ data and a non-Matthiessen's impurity scattering behavior.

Figure 14 shows temperature derivatives of the ambient pressure in-plane resistivity data presented in Fig. 4. Two CDW transitions are seen in the derivatives, although the signature of CDW2 fades for lower values of x .

APPENDIX C: DERIVATIVES OF THE IN-PLANE AND c -AXIS TEMPERATURE DEPENDENT RESISTIVITY OF $\text{LaAu}_{0.970}\text{Sb}_2$ UNDER PRESSURE

Figure 15 shows the temperature derivatives of data in Fig. 6, i.e., of the temperature-dependent (a) in-plane, (b) c -axis resistivity of $\text{LaAu}_{0.970}\text{Sb}_2$ measured at different pressures. Note that for $P = 0$ both CDW1 and CDW2 can

be seen in $d\rho_{ab}/dT$ data although the feature associated with CDW2 is weak. T_{CDW1} is clearly discernible under pressure, until suppressed to $T = 0$ K. Both CDW transitions can be detected in the $d\rho_c/dT$ data until they are driven to $T = 0$ K under pressure.

APPENDIX D: LOW TEMPERATURE RESISTIVITY OF $\text{LaAu}_{0.970}\text{Sb}_2$ UNDER PRESSURE

For traditional, antiferromagnetic quantum critical points [47,48] the evolution of low temperature exponent of the temperature dependent resistivity (n in $\rho(T) = \rho_0 + AT^n$) from Fermi-liquid-like behavior, $n = 2$ far from a QCP to non-Fermi-liquid behavior $n \neq 2$ (often $n = 1$ or $n = 1.5$) presents one of the signs of a strange metal behavior in proximity to QCP. In Fig. 16 the evolution of the exponents n under pressure for in-plane and c -axis resistivity of LaAu_xSb_2 is presented. Several observations are noteworthy. Although close, all exponents differ from a simple Fermi liquid $n = 2$. It appears that for the low temperature exponent of ρ_{ab} under pressure, an anomalous behavior is seen at P_{CDW1} , whereas for the c -axis data the anomaly is observed around P_{CDW2} [the maximum pressure of the $\rho_c(T, P)$ run is close or below P_{CDW1}]. The CDW QCPs in LaAu_xSb_2 under pressure

TABLE III. EDS results for LaAu_xSb_2 samples grown using different starting compositions.

Sample	La at. %	Au at. %	Sb at. %	Au/La	2Au/Sb	3Au/(La + Sb)
Au1	26.41(9)	23.09(4)	50.64(8)	0.874(4)	0.912(3)	0.899(4)
Au2	26.1(2)	23.9(1)	50.1(1)	0.92(1)	0.954(7)	0.941(9)
Au4	25.8(1)	24.49(4)	49.9(1)	0.951(5)	0.982(4)	0.971(5)
Au6	25.9(2)	24.55(4)	49.61(7)	0.949(8)	0.990(3)	0.976(6)
Au8	25.71(4)	24.65(7)	49.70(7)	0.959(4)	0.992(4)	0.981(7)

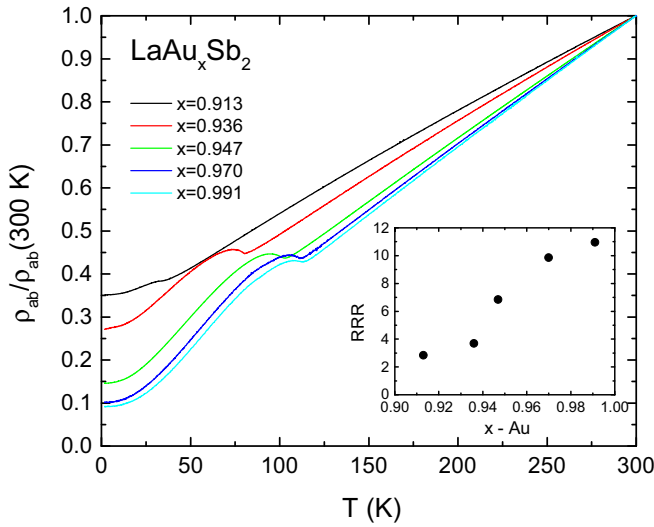


FIG. 13. Temperature-dependent, in-plane, resistivity data for LaAu_xSb_2 samples normalized to that of the $T = 300\text{ K}$ values. Inset: residual resistivity ratio values plotted as a function of x -Au.

are not expected to present a textbook example, since only reasonably small parts of the Fermi surface are gapped as a result of CDWs, whereas the electrical transport is determined by contributions from multiple Fermi surface sheets. These multiple sheets and multiple scattering times associated with them might be the reason for the observed deviation from $n = 2$ in low temperature resistivity far from CDW QCP.

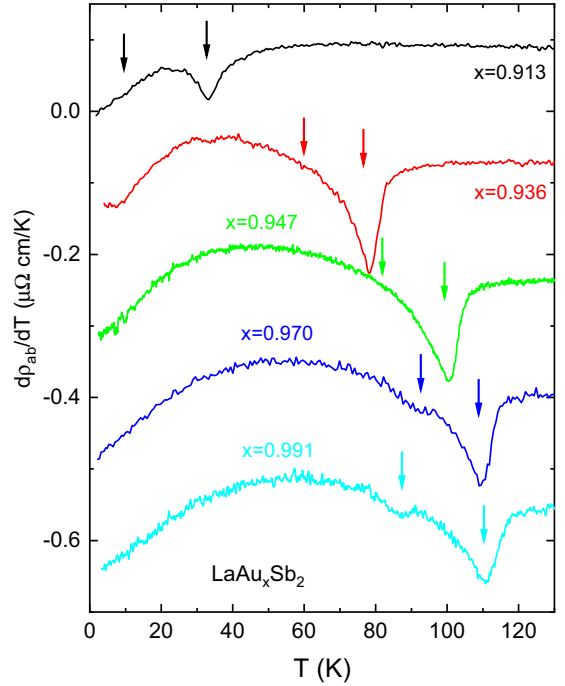


FIG. 14. Temperature derivatives of the in-plane resistivity data for LaAu_xSb_2 samples (based on the $\rho_{ab}(T)$ from Fig. 4). The data are shifted vertically for clarity. Arrows mark CDW transitions.

APPENDIX E: MAGNETORESISTANCE OF $\text{LaAu}_{0.970}\text{Sb}_2$ UNDER PRESSURE

Figure 17 presents transverse magnetoresistance $[\rho(H) - \rho(H = 0)]/\rho(H = 0)$ of $\text{LaAu}_{0.970}\text{Sb}_2$ at 1.8 K measured

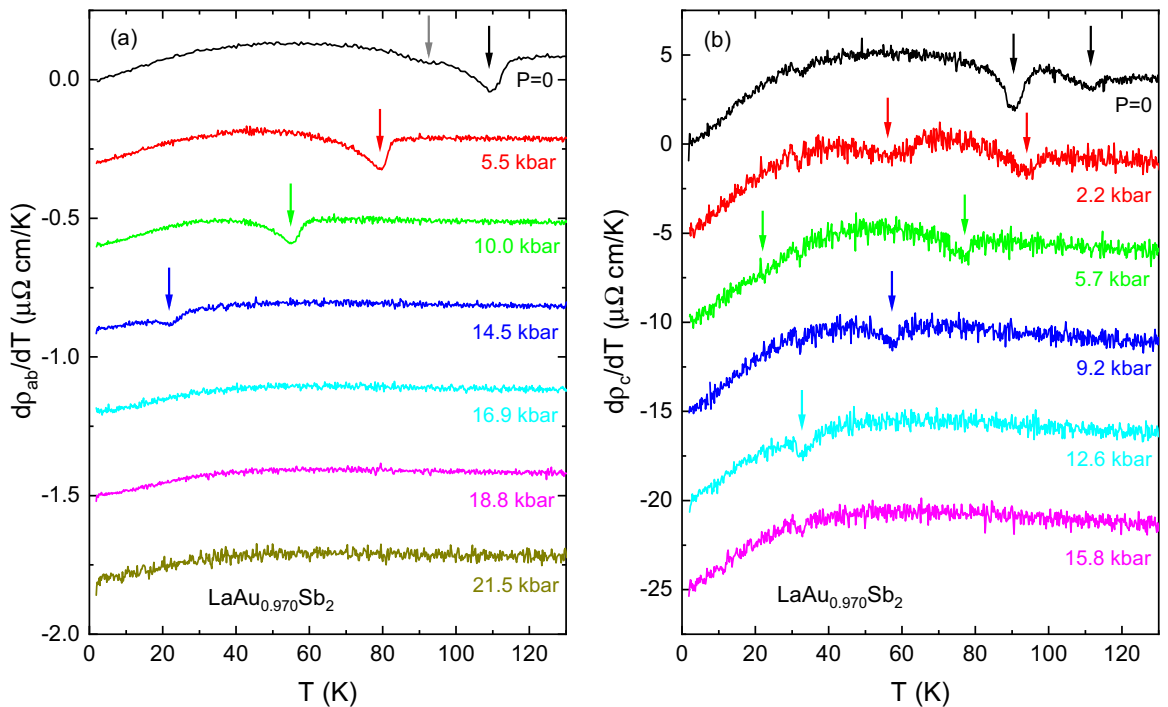


FIG. 15. Temperature derivatives of (a) in-plane and (b) c -axis resistivity of $\text{LaAu}_{0.970}\text{Sb}_2$ under pressure. The data are shifted vertically for clarity. Arrows mark CDW transitions.

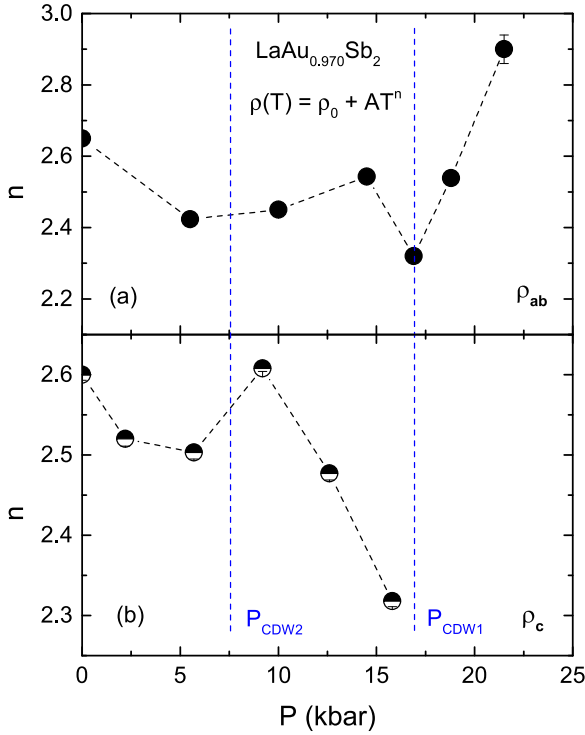


FIG. 16. Low temperature resistivity exponent n , in $\rho(T) = \rho_0 + AT^n$ fits of the data from 1.8 K to 15 K for (a) in-plane and (b) c -axis resistivity measurements plotted as a function of pressure. Dashed lines are a guide for the eye. Vertical dashed lines mark critical pressures for CDW1 and CDW2.

(a) for $I||ab, H||c$ under pressure up to 21.5 kbar, and (b) for $I||c, H||ab$ under pressure up to 15.8 kbar plotted on a log-log scale. The slopes obtained in linear fits of these data (dashed lines) give the values of the exponent α in $\Delta\rho/\rho_0 \propto H^\alpha$. The fits were performed in the magnetic field range between ~ 20 and 140 kOe.

APPENDIX F: $\text{LaAu}_{0.936}\text{Sb}_2$ UNDER PRESSURE

In-plane resistivity under pressure has been measured for $\text{LaAu}_{0.936}\text{Sb}_2$ for comparison to earlier literature as well as for comparison to the $\text{LaAu}_{0.970}\text{Sb}_2$ shown in the main text. The results are presented in Fig. 18. As for $\text{LaAu}_{0.970}\text{Sb}_2$, resistivity decreases under pressure and the CDW1 transition is suppressed. We were not able to follow the CDW2 under pressure most probably because it was already suppressed to $T = 0$ K by 4.5 kbar. The pressure derivative of T_{CDW1} is $-7.8(1)$ K/kbar, so the suppression of the T_{CDW1} is faster than in the case of $\text{LaAu}_{0.970}\text{Sb}_2$ and LaAgSb_2 . Linear extrapolation suggests that the critical pressure for CDW1 in $\text{LaAu}_{0.936}\text{Sb}_2$ is ≈ 10 kbar.

Effect of pressure on the resistivity of $\text{LaAu}_{0.936}\text{Sb}_2$ at the base temperature, 1.8 K, and above the CDW transitions, at 250 K, is shown in Fig. 19. At 250 K resistivity decreases with the rate of $1/\rho_0 d\rho/dP = -0.008(1)$ 1/K, which is close to the data for LaAgSb_2 [26] and $\text{LaAu}_{0.970}\text{Sb}_2$ in the same temperature range. Similar to $\text{LaAu}_{0.970}\text{Sb}_2$, resistivity

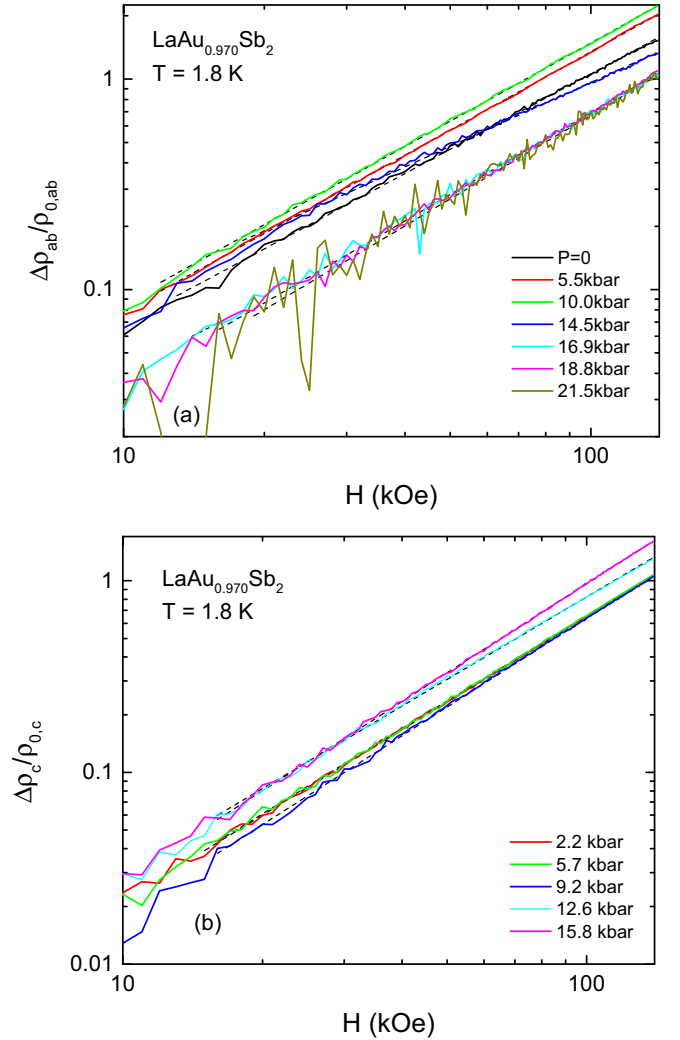


FIG. 17. (a) Transverse magnetoresistance of $\text{LaAu}_{0.970}\text{Sb}_2$ at 1.8 K plotted on a log-log scale (a) $I||ab, H||c$ measured up to 21.5 kbar, (b) $I||c, H||ab$ up to 15.8 kbar. Dashed lines are linear fits.

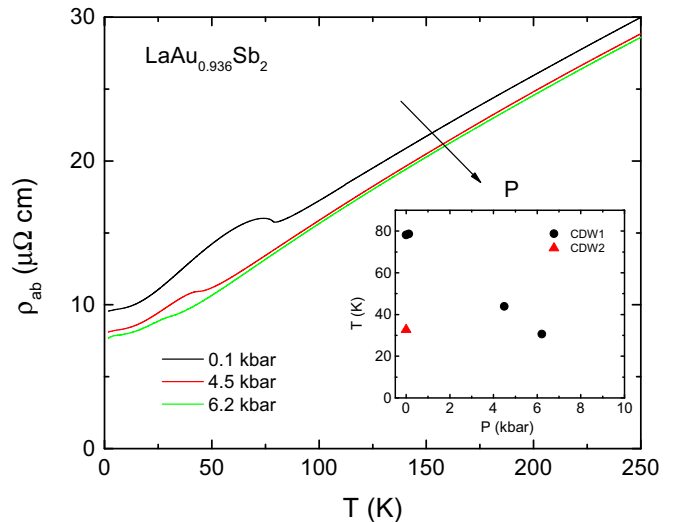


FIG. 18. In-plane resistivity of $\text{LaAu}_{0.936}\text{Sb}_2$ under pressure. Arrow points to the direction of pressure increase. Inset: change of CDW temperatures under pressure.

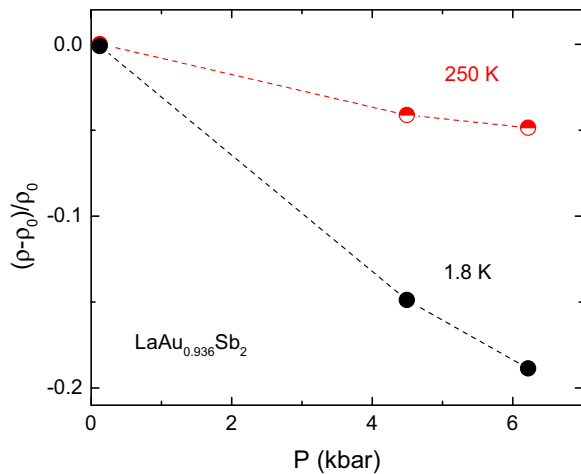


FIG. 19. Relative change of in-plane resistivity of $\text{LaAu}_{0.936}\text{Sb}_2$ at 250 K and 1.8 K under pressure.

measured at 1.8 K initially is decreasing significantly faster [$1/\rho_0 d\rho/dP = -0.031(2) \text{ 1/K}$] than at 250 K.

APPENDIX G: EFFECTS OF PHYSICAL AND CHEMICAL PRESSURE ON CDW TEMPERATURES OF LaAu_xSb_2

The unit cell volume of LaAu_xSb_2 decreases with decrease of x , so some chemical pressure is exerted. To compare physical and chemical pressure effects in the LaAu_xSb_2 family, the charge density wave temperatures for CDW1 and CDW2 are plotted as a function of the unit cell volume for different LaAu_xSb_2 samples at ambient pressure (e.g., under chemical pressure), as well as for $\text{LaAu}_{0.970}\text{Sb}_2$ and $\text{LaAu}_{0.936}\text{Sb}_2$ under pressure in Fig. 20. For chemical pressure the unit cell volume is taken from the Table I, and for physical pressure the unit cell volumes were calculated using the elastic constants measured for a sister compound, LaAgSb_2 [24].

Whereas both chemical and physical pressure cause decrease of CDW1 and CDW2 temperatures, there are some differences. The chemical pressure appears to have stronger, and non-linear effect of CDW temperatures, that suggests measurable effects of additional contributions, namely disorder and possible change of the band filling in LaAu_xSb_2 samples with different values of x .

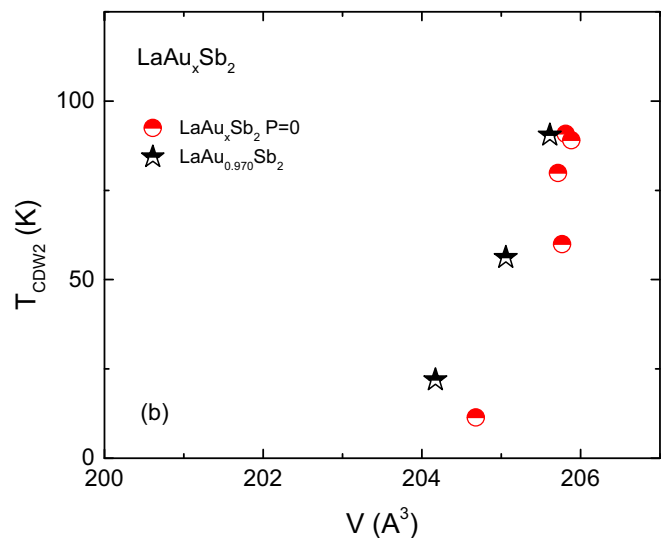
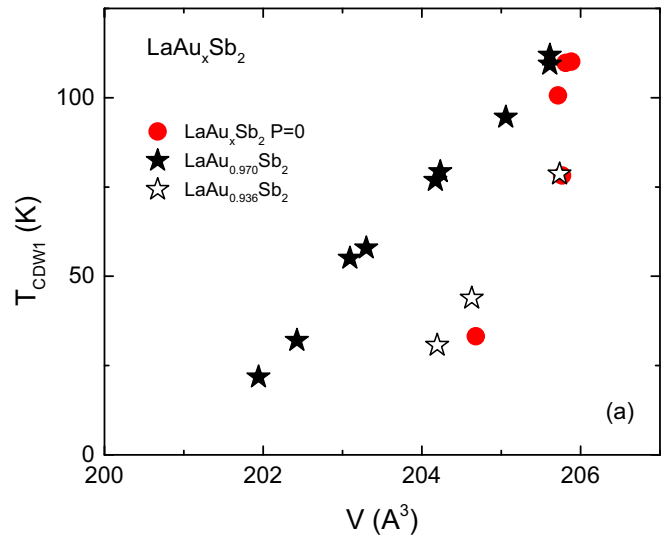


FIG. 20. (a) T_{CDW1} and (b) T_{CDW2} as a function of the unit cell volume for LaAu_xSb_2 with different x at ambient pressure (red circles) and for $\text{LaAu}_{0.970}\text{Sb}_2$ and $\text{LaAu}_{0.936}\text{Sb}_2$ under pressure (black stars).

Altogether the issue of equivalence of chemical and physical pressure in RTSb_2 (R = rare earth, T = transition metal) family appears to be complex and is discussed in more detail in Refs. [25,26,49].

- [1] M. D. Johannes and I. I. Mazin, *Phys. Rev. B* **77**, 165135 (2008).
- [2] H.-M. Eiter, M. Lavagnini, R. Hackl, E. A. Nowadnick, A. F. Kemper, T. P. Devereaux, J.-H. Chu, J. G. Analytis, I. R. Fisher, and L. Degiorgi, *Proc. Natl. Acad. Sci. U.S.A.* **110**, 64 (2013).
- [3] X. Zhu, Y. Cao, J. Zhang, E. W. Plummer, and J. Guo, *Proc. Natl. Acad. Sci. U.S.A.* **112**, 2367 (2015).
- [4] J.-P. Pouget, *C. R. Phys.* **17**, 332 (2016).
- [5] M. Saint-Paul and P. Monceau, *Adv. Condens. Matter Phys.* **2019**, 2138264 (2019).
- [6] G. Bilbro and W. L. McMillan, *Phys. Rev. B* **14**, 1887 (1976).
- [7] C. A. Balseiro and L. M. Falicov, *Phys. Rev. B* **20**, 4457 (1979).
- [8] K. Machida, T. Kōyama, and T. Matsubara, *Phys. Rev. B* **23**, 99 (1981).
- [9] A. M. Gabovich, A. I. Voitenko, J. F. Annett, and M. Ausloos, *Supercond. Sci. Technol.* **14**, R1 (2001).
- [10] B. Wang, Y. Liu, X. Luo, K. Ishigaki, K. Matsubayashi, W. Lu, Y. Sun, J. Cheng, and Y. Uwatoko, *Phys. Rev. B* **97**, 220504(R) (2018).
- [11] R. Peierls, *Ann. Phys.* **396**, 121 (1930).

- [12] R. E. Peierls, *Quantum Theory of Solids* (Clarendon Press, Oxford, 1955).
- [13] H. Fröhlich, *Proc. R. Soc. A* **223**, 296 (1954).
- [14] M. Brylak, M. H. Möller, and W. Jeitschko, *J. Solid State Chem.* **115**, 305 (1995).
- [15] O. Sologub, H. Noël, A. Leithe-Jasper, P. Rogl, and O. I. Bodak, *J. Solid State Chem.* **115**, 441 (1995).
- [16] K. D. Myers, S. L. Bud'ko, I. R. Fisher, Z. Islam, H. Kleinke, A. H. Lacerda, and P. C. Canfield, *J. Magn. Magn. Mater.* **205**, 27 (1999).
- [17] C. Song, J. Park, J. Koo, K.-B. Lee, J. Y. Rhee, S. L. Bud'ko, P. C. Canfield, B. N. Harmon, and A. I. Goldman, *Phys. Rev. B* **68**, 035113 (2003).
- [18] C. S. Lue, Y. F. Tao, K. M. Sivakumar, and Y. K. Kuo, *J. Phys.: Condens. Matter* **19**, 406230 (2007).
- [19] S. L. Bud'ko, S. A. Law, P. C. Canfield, G. D. Samolyuk, M. S. Torikachvili, and G. M. Schmiedeshoff, *J. Phys.: Condens. Matter* **20**, 115210 (2008).
- [20] E. D. Mun, S. L. Bud'ko, and P. C. Canfield, *J. Phys.: Condens. Matter* **23**, 476001 (2011).
- [21] R. Y. Chen, S. J. Zhang, M. Y. Zhang, T. Dong, and N. L. Wang, *Phys. Rev. Lett.* **118**, 107402 (2017).
- [22] K. Wang and C. Petrovic, *Phys. Rev. B* **86**, 155213 (2012).
- [23] X. Shi, P. Richard, K. Wang, M. Liu, C. E. Matt, N. Xu, R. S. Dhaka, Z. Ristic, T. Qian, Y.-F. Yang, C. Petrovic, M. Shi, and H. Ding, *Phys. Rev. B* **93**, 081105(R) (2016).
- [24] S. L. Bud'ko, T. A. Wiener, R. A. Ribeiro, P. C. Canfield, Y. Lee, T. Vogt, and A. H. Lacerda, *Phys. Rev. B* **73**, 184111 (2006).
- [25] S. Masubuchi, Y. Ishii, K. Ooiwa, T. Fukuhara, F. Shimizu, and H. Sato, *JPS Conf. Proc.* **3**, 011053 (2014).
- [26] M. S. Torikachvili, S. L. Bud'ko, S. A. Law, M. E. Tillman, E. D. Mun, and P. C. Canfield, *Phys. Rev. B* **76**, 235110 (2007).
- [27] S. Seo, V. A. Sidorov, H. Lee, D. Jang, Z. Fisk, J. D. Thompson, and T. Park, *Phys. Rev. B* **85**, 205145 (2012).
- [28] C. N. Kuo, D. Shen, B. S. Li, N. N. Quyen, W. Y. Tzeng, C. W. Luo, L. M. Wang, Y. K. Kuo, and C. S. Lue, *Phys. Rev. B* **99**, 235121 (2019).
- [29] K. D. Myers, S. L. Bud'ko, V. P. Antropov, B. N. Harmon, P. C. Canfield, and A. H. Lacerda, *Phys. Rev. B* **60**, 13371 (1999).
- [30] L. Zhao, E. A. Yelland, J. A. N. Bruin, I. Sheikin, P. C. Canfield, V. Fritsch, H. Sakai, A. P. Mackenzie, and C. W. Hicks, *Phys. Rev. B* **93**, 195124 (2016).
- [31] P. C. Canfield, T. Kong, U. S. Kaluarachchi, and N. H. Jo, *Philos. Mag.* **96**, 84 (2016).
- [32] *Standard Reference Material 676a*, NIST (2015).
- [33] S. L. Bud'ko, A. N. Voronovskii, A. G. Gapotchenko, and E. S. Itskevich, *Zh. Eksp. Teor. Fiz.* **86**, 778 (1984) [*Sov. Phys. JETP* **59**, 454 (1984)].
- [34] S. K. Kim, M. S. Torikachvili, E. Colombier, A. Thaler, S. L. Bud'ko, and P. C. Canfield, *Phys. Rev. B* **84**, 134525 (2011).
- [35] M. S. Torikachvili, S. K. Kim, E. Colombier, S. L. Bud'ko, and P. C. Canfield, *Rev. Sci. Instrum.* **86**, 123904 (2015).
- [36] A. Eiling and J. S. Schilling, *J. Phys. F* **11**, 623 (1981).
- [37] E. S. Itskevich, *Cryogenics* **4**, 365 (1964).
- [38] E. S. Itskevich, A. N. Voronovskii, A. F. Gavrilov, and V. A. Sukhparov, *Cryogenics* **7**, 359 (1967).
- [39] J. D. Thompson, *Rev. Sci. Instrum.* **55**, 231 (1984).
- [40] A. C. Larson and R. B. Von Dreele, Technical Report No. LAUR 86-748, Los Alamos National Laboratory, 2000.
- [41] B. H. Toby, *J. Appl. Crystallogr.* **34**, 210 (2001).
- [42] C. Kittel, *Introduction to Solid State Physics*, 8th ed. (Wiley, Hoboken, NJ, 2005), p.150.
- [43] H. G. Schuster, *Solid State Commun.* **14**, 127 (1974).
- [44] L. N. Bulaevskii and M. V. Sadovskii, *Fiz. Tverd. Tela* **16**, 1159 (1974).
- [45] L. N. Bulaevskii, *Usp. Fiz. Nauk* **120**, 259 (1976) [*Sov. Phys. Usp.* **19**, 836 (1976)].
- [46] G. Gómez-Santos and F. Ynduráin, *Phys. Rev. B* **29**, 4459 (1984).
- [47] G. R. Stewart, *Rev. Mod. Phys.* **73**, 797 (2001).
- [48] G. R. Stewart, *Rev. Mod. Phys.* **78**, 743 (2006).
- [49] L. Xiang, D. H. Ryan, P. C. Canfield, and S. L. Bud'ko (unpublished).